Research Square

Preprints are preliminary reports that have not undergone peer review.
They should not be considered conclusive, used to inform clinical practice,
or referenced by the media as validated information.

Effects of Cr-Coatings on Hydride Reorientation in Zircaloy-4 Claddings

Aaron W. Colldeweih

aaron.colldeweih@inl.gov

Idaho National Laboratory

Dahyeon Woo

Seoul National University

Aaron Craft

Idaho National Laboratory

Malachi M. Nelson

Idaho National Laboratory

Nathan Capps

Oak Ridge National Laboratory

Pavel Trtik

Villigen PSI

Woo Hyun Jung

University of Nevada

David W. Kamerman

Idaho National Laboratory

Article

Keywords:

Posted Date: November 12th, 2026

DOI: https://doi.org/10.21203/rs.3.rs-11529859/v1

License: This work is licensed under a Creative Commons Attribution 4.0 International License.
Read Full License

Additional Declarations: No competing interests reported.

Effects of Cr-Coatings on Hydride Reorientation in Zircaloy-4 Claddings

Aaron W. Colldeweih[1,*], Dahyeon Woo[5], Aaron Craft[1], Malachi M. Nelson[1], Nathan Capps[2], Pavel Trtik[3], Woo Hyun Jung[4], David W. Kamerman[1]

[1]Idaho National Laboratory, Idaho Falls, Idaho, USA

[2]Oak Ridge National Laboratory, Oak Ridge, Tennessee, USA

[3]PSI Center for Neutron and Muon Science, Paul Scherrer Institute, 5232 Villigen PSI, Switzerland

[4]University of Nevada, Las Vegas, Las Vegas, Nevada, USA

[5]Seoul National University, Seoul, South Korea

*Corresponding author: Aaron Colldeweih, aaron.colldeweih@inl.gov

1 Abstract

The effect of reoriented hydrides in chromium coated Zircaloy-4 alloys using cold spray and physical vapor deposition methods was compared to uncoated Zircaloy-4, a reference light water reactor cladding material. The reorientation studies were carried out in an internal pressurization assembly inside of a furnace under conditions resembling pellet cladding mechanical interactions. The morphology of the reoriented hydrides of the bare coating was consistent with reorientation tests that can be found in literature. At elevated strains above 0.3% hoops strain, the chromium coated tubes formed small cracks in the hard chromium layer which led to localized stress concentrations that ultimately caused the precipitation of radially oriented hydrides at crack tips. Through high-resolution neutron radiography, spatially-resolved hydrogen concentration was characterized in the cladding. Large gradients the hydrogen concentration were observed in chromium coated cladding compared to the relatively homogenous distribution of the bare cladding. Furthermore, through ring compression testing, the resulting mechanical response to of bare versus chromium coated cladding with radial hydrides was demonstrated. Specifically, localized radial hydrides at coating cracks caused multiple shallow locations of cladding cracking where the bare material cracked more catastrophically due to the higher connectivity of radial and circumferential hydrides.

2 Introduction

Zircaloy fuel cladding represents the primary barrier to fission product release in light water reactors which currently account for most nuclear power reactors in the United States and across the world [1]. The cladding system must balance thermal, mechanical, chemical, and neutronic performance, and its structural stability is essential for operational, anticipated, and accident scenarios. After the Fukushima accident, Accident Tolerant Fuel (ATF) concepts were developed primarily to increase cladding survivability in high-temperature steam environments and reduce hydrogen production [2-4]. Among those concepts, chromium (Cr) -coated Zircaloy claddings are the nearest term solution for pressurized water reactors [1-5]. Cr-coatings are typically 8-50 um thick to provide a balance of corrosion, mechanical, and neutronic performance [5]. Cr-coatings are primarily deposited using cold spray (CS) or physical vapor deposition (PVD) techniques. Both techniques lead to unique coating-cladding interfaces and microstructural properties [5, 6]. The extreme plastic deformation involved in CS methods results in microstructure with tortuous grain boundaries and interface properties [6, 7]. The PVD method retains a relatively smooth cladding interface nucleating smaller grains that quickly transition into larger columnar grains with relatively straight grain boundaries [8]. While both produce unique microstructural characteristics, both coatings have demonstrated excellent protectiveness and cladding adherence. Nevertheless, the chromium layer of both concepts have harder mechanical properties than the underlying zirconium alloy.

Cr-coatings not only resist high-temperature steam oxidation, but also oxidation and hydrogen pickup during normal operations that can limit the overall cladding lifetime [7, 9-12]. More specifically, zirconium alloys absorb hydrogen during normal in-reactor operation primarily through the dissociation of hydrogen resulting from the oxidation of the cladding. The hydrogen will form brittle zirconium hydrides once the solubility limit is exceeded. However, Zircaloy's hexagonal close packed (HCP) structure promotes hydride precipitation on basal planes as a result of the pilgered texture with basal normals generally aligned with the radial direction [13] [14]. This texture strengthens the cladding in the radial direction to resist thinning and helps prevent hydrides from forming in the radial orientation [14]. Radial hydrides are particularly detrimental to cladding because they enhance hydride connectivity and enhance through-wall propagation leading to premature failure [15-17]. However, while Zircaloy's texture prevents radial hydrides under nominal conditions, elevated tensile stresses, such as those generated during pellet–cladding mechanical interaction (PCMI), can reorient hydrides in the radial direction increasing the likelihood of brittle failure. The stress sensitivity of hydrogen migration at elevated temperature also causes the hydrides to change orientation based on the principal

stresses in the material [18, 19]. Thus, the stress state used to emulate PCMI conditions is especially important in the context of hydride evolution and interplay with cracks in the Cr-coating, which are also sensitive to the stress state [8]. During PCMI-like loading, both CS and PVD coatings can develop axial cracks once critical strain levels are exceeded [20, 21] [22, 23]. Moreover, localized stress concentrations, such as crack tips, can lead to localized hydride precipitation increasing the vulnerability of the system [20].

Initial studies have investigated the effects of Cr-coating cracks on hydride formation and reorientation [20]. This work builds on the previous studies and investigates hydride evolution of various concepts of Cr-coated Zircaloy cladding when exposed to hydride reorientation conditions. Furthermore, this work compares the bare Zircaloy cladding to demonstrate baseline effects of hydride reorientation. Samples subjected to reorientation testing were characterized by using optical microscopy and neutron radiography to characterize the hydrogen concentration and localization. Optical microscopy and neutron radiography are ideal techniques for identifying and quantifying the hydrogen distribution throughout zirconium alloy cladding [16, 24]. Ring compression testing (RCT) was used to compare the mechanical responses of the cladding concepts after reorientation testing. RCT is an effective way to demonstrate the brittle nature of tube material, as shown in other works investigating hydride reorientation [25, 26] [27].

3 Materials

3.1 Zircaloy-4

The base cladding material for both material was Zircaloy-4 (Zry-4) cladding conforming to ASTM B353 [28]. The Zry-4 cladding was procured through two different commercial suppliers. Samples are sectioned into 150 mm lengths following their respective coating application.

3.2 Uncoated and CS Cr-Coated Cladding

The base Zry-4 used for uncoated and CS coating is cold-worked, stress-relieved Zry-4. For the CS coated cladding, tubes were cleaned as described in [33]. The CS Cr-coating technique is performed at the University of Wisconsin, Madison according to the parameters shown in Table 1**.** After deposition, the cold spray coatings are polished to a thickness of 20 µm using a rotary lathe and 800 grit SiC abrasive paper. The CS coating is thicker than the PVD coating to reflect industry practice and comparison to representative cladding systems considered at high technical readiness [29, 30]. The resulting outer diameter of the tubes were 9.5 mm with a wall thickness of 0.57 mm.

Table 1: Parameters used for cold spray deposition of Cr on Zr-4 cladding substrates.

Gas Composition	Gas Temperature	Gas Pressure	Gun Traverse Speed	Rotary Lathe Speed	Gas Flow Rate
100% N_2	750° C	38 bar	3.4 mm/s	400 RPM	80 m^3/hr

3.3 PVD Cr-Coated Cladding

The base Zry-4 used for PVD coating was stress relief annealed. Before coating, the surfaces of the tubes are plasma etched and cleaned, which removes a minimal amount of material from the outer diameter. The PVD Cr-coating technique employs a high power impulse magnetron sputtering (HiPIMS) system to deposit a 9 μm nominal thickness which has been characterized in detail in other work [31]. A 9 μm thickness is chosen to provide high-temperature corrosion benefits (e.g., act as a barrier to steam oxidation and loss of mechanical strength of the Zry-4 substrate) while minimally affecting the composite tube's baseline mechanical performance [32]. This parameter also reflects leading commercial materials using the PVD technique [5, 32-35]. The bias voltage is reduced throughout the deposition process to ensure coating uniformity, and the resulting outer diameters of the tubes are between 9.25-9.30 mm with a wall thickness of 0.5 mm. Microstructure characterization of the base Zry-4 cladding used for PVD samples can be found in [36].

4 Methods

4.1 Hydrogen Charging

The cladding tubes are charged with hydrogen using a gaseous Seivert's technique. Specimens are sealed in a quartz tube and vacuum (~ 2E-9 psia) is applied before charging the environment with high purity hydrogen (~ 5 psia). The quartz tube environment is isolated and enclosed in a furnace where it is heated to 400 °C to ensure homogenous hydrogen distribution. Further details on the technique and equipment used can be found in the following reference [37], where targeted hydrogen charging was achieved.

Tubes with a Cr-coating were polished and cleaned on the inner surface to allow hydrogen uptake using Methods 5 and 2 from prior work [37]. The uncoated claddings are prepared using the same methods on both the inner and outer surfaces. Previous work shows that hydrogen uptake primarily occurs through the inner surface of Cr-coated claddings using this method because the Cr-coating protects the outer surface. This uptake path is opposite to reactor conditions; however, reference segments of the materials were characterized to demonstrate uniform hydrogen uptake using this procedure. The as-

charged material can be found in the Supplementary Materials (Figure 16) highlighting a uniform hydride distribution.

4.2 Reorientation Tests

The mechanical testing system used to perform the hydride reorientation tests applies internal pressure to replicate bi-axial stress conditions in the cladding consistent with PCMI [38]. The testing system shown in Figure 1 uses a control feedback loop to apply internal pressure at a monotonic strain rate to measure elastic constants and yield behavior. Cladding tubes were capped but unconstrained at the top and are fixed to the stationary bulkhead at the bottom to allow argon gas to pressurize the sample and ensure a biaxial stress state (transverse and axial). Transverse and axial extensometers measure strain with the transverse signal used for feedback control. Further description of this system and more detailed description of methods are included in [38].

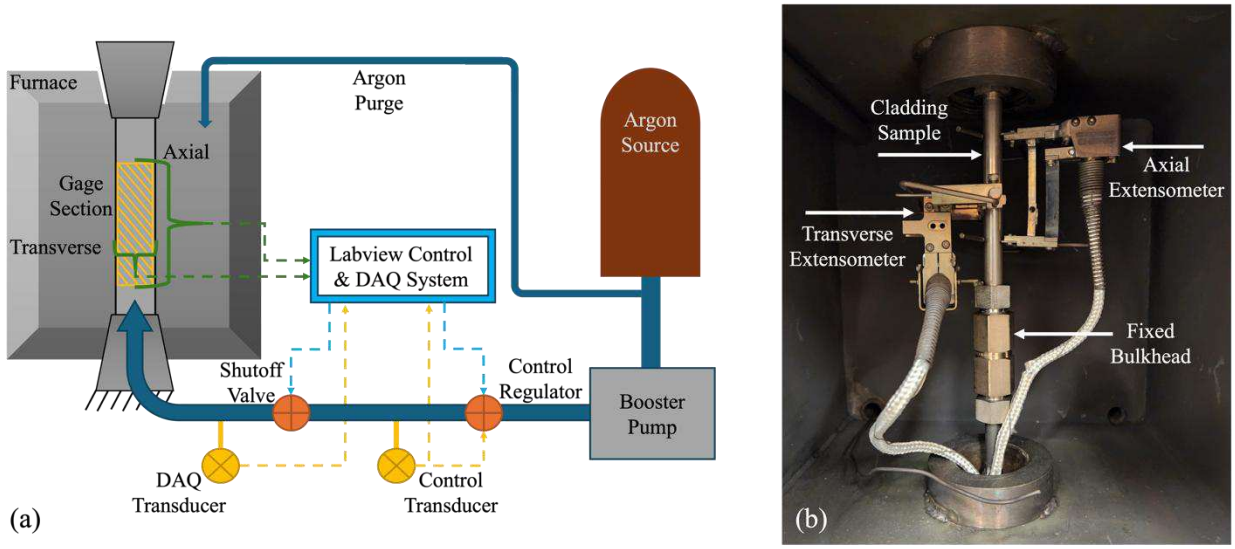


Figure 1: Experimental system used for monotonic strain-rate internal pressure loading. (a) Schematic diagram of loading system. (b) Photograph of sample with extensometers mounted inside furnace.

Samples are enclosed in the furnace and heated to 350 °C in an argon atmosphere. Then, cladding tubes are pressurized in strain control mode with a 0.1 %/min hoop strain rate to achieve the desired strains shown in Table 2. While holding the hoop strain constant, the sample is cooled at 10 °C/hr to simulate a reactor shut down from hot zero power to cold zero power. Once the sample temperature reaches 100 °C, the test is considered finished and system is vented. The tests ranged from small hoop strains of 0.3% to investigate reorientation prior to crack onset, 0.5% hoop strain to investigate reorientation just after crack onset, and up to the 1% hoop strain at the regulatory limits for total cladding strain

[39]. Following hydride reorientation tests, specimens are sectioned and prepared for optical microscopy according to methods included in the Specimen Preparation of Supplementary Materials.

Table 2: Test matrix for testing presenting hoop strain maintained during hydride reorientation of the bare, PVD coated and CS coated tubes.

		Test		
	Concept	**1**	**2**	**3**
Hoop Strain (%)	**Bare**	0.3	0.5	1.0
	PVD	0.3	0.5	1.0
	CS	0.3	0.5	1.0

4.3 Neutron Radiography

The primary objective of the radiography is to determine localized regions of hydrogen uptake, particularly near the coating-cladding interface where anticipated localizations of radial hydrides might have formed after reorientation testing. Neutron radiography is an ideal technique for charactering local hydrogen concentrations in zirconium because the large neutron cross section of hydrogen compared to that of zirconium. Many previous studies have demonstrated hydrogen concentration characterization within the liner material of zircaloy claddings as well as local hydrogen concentrations around delayed hydride crack tips [16, 24, 40-42]. The details of the image acquisition and camera details can be found in the following reference [23]. Further details of the image processing and calibration techniques can be found in the following reference [16]. This work is based on experiments performed at the Swiss spallation neutron source SINQ, Paul Scherrer Institute, Villigen, Switzerland using the Neutron Microscope detector [43] at ICON beamline [44], SINQ, PSI [45]. The camera used was an Andor iKon-L CCD with the isotropic pixel size of the resulting image equal to 2.7 um.

A MATLAB-based analysis tool named Neutron Radiograph Inference of Concentration of Hydrogen (NRICH) was developed to automatically mask the sample area and analyze high-resolution neutron radiographs. The open-source code and manual is publicly available on GitHub and in supplemental information. Using NRICH, both the overall

average hydrogen concentration and the radial concentration profiles within the cladding can be quantitatively evaluated. Furthermore, local spatial variations are visualized through contour plots, demonstrating preferential regions (inner or outer wall) and directional growth (circumferential or radial) for hydride precipitation.

4.4 Ring Compression Tests

The mechanical response of the hydride-reoriented specimens is evaluated using ring compression tests (RCT). An Instron 5966 testing machine compresses each ~8-mm long specimen at a constant displacement rate of 0.1 mm/s at room temperature (25 °C). The tests are terminated once a significant load drop exceeding 40% of the maximum load occurred. A compliance correction is applied to the raw displacement-load curves to account for the inherent test fixture deflection. The compliance calibration used a stiff specimen to measure the linear region up to 500 N to interpolate compliance of forces which remain below that value in this study. The actual specimen displacement is calculated by subtracting the machine displacement at the corresponding load from the measured total displacement. The load is then normalized by the specimen length to obtain the load per unit length (N/mm). The mechanical characteristics including yielding behavior and subsequent load drops are identified from the resulting curves to assess the ductility and fracture resistance of the cladding. An exemplary RCT load-displacement curve is presented in Figure 18, featuring dual y-axes where the left axis represents the raw load and the right axis indicates the load per unit length calculated by dividing the load by the 8-mm tube specimen height. On this curve, the fracture point is explicitly designated at the location where the sudden load drop exceeds the 40% threshold. The mechanical characteristics including yielding behavior and subsequent load drops are identified from the resulting curves to assess the ductility and fracture resistance of the cladding.

5 Test Results

5.1 Reorientation Tests

The cladding tubes subjected to hydride reorientation were first analyzed through metallography. The metallographs revealed that small cracks had formed in the Cr-coating of coated cladding and hydrides of the bare cladding. Figure 2 presents the optical micrographs of radial cross sections taken from each of the reorientation tests. Figure 3 presents the crack counts for each of the samples. It is notable that each of the strain conditions produced radially oriented hydrides while circumferential hydrides are also present. Most notable are the radial hydrides that have formed at the crack tips of the

cracked Cr-coatings. Figure 4 shows the results of the Radial Hydride Fraction (RHF) analysis performed using the PROPHET code [46], with the hydride rim regions excluded from the image analysis to ensure accuracy. In these processed images, circumferential hydrides are marked with green lines and radial hydrides with red lines, with the calculated RHF values indicated below each optical micrograph.

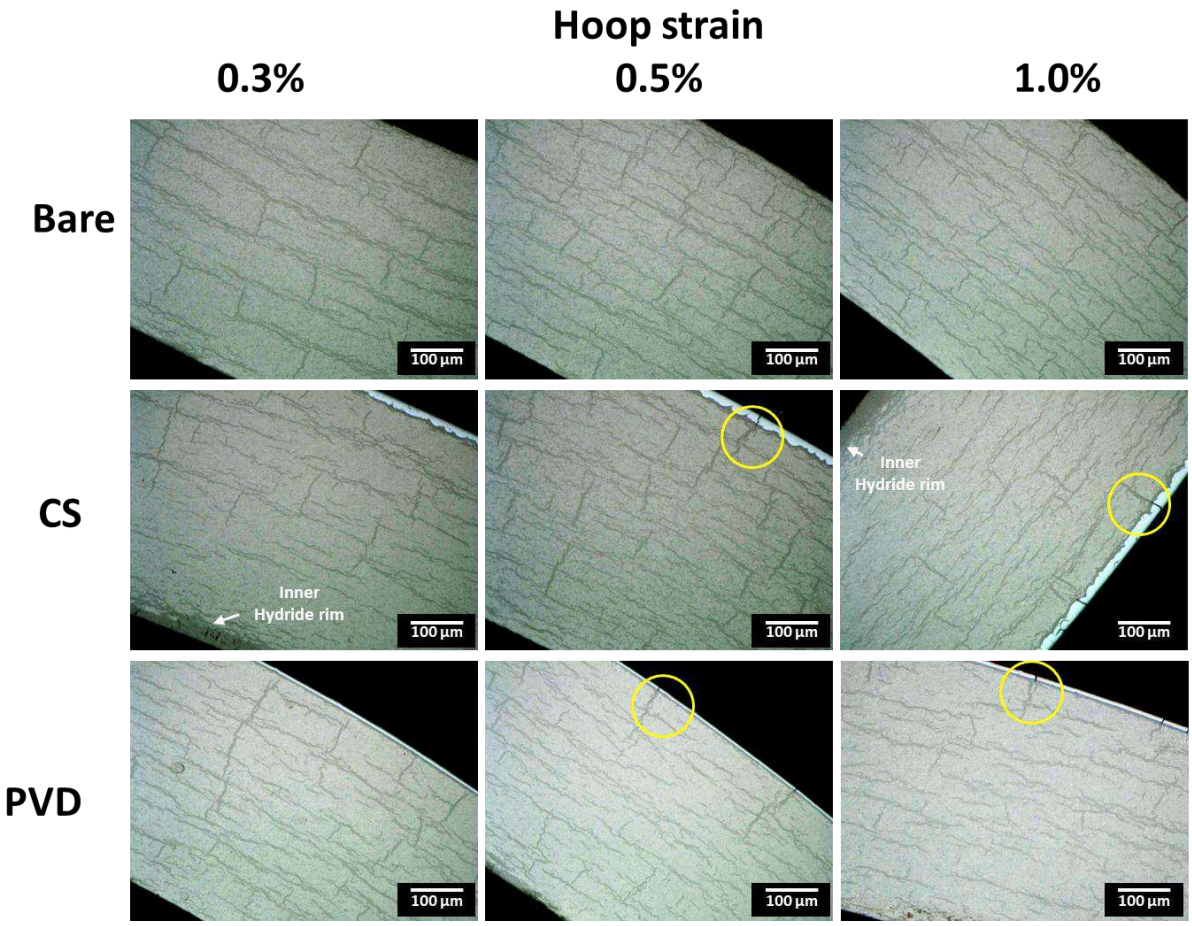


Figure 2: Optical micrographs of the radial cross section from the bare, CS, and PVD coated claddings after reorientation testing. The yellow circles highlight the regions of the cracked

coatings. Micrographs are representative of the state of hydride reorientation prior to RCT tests.

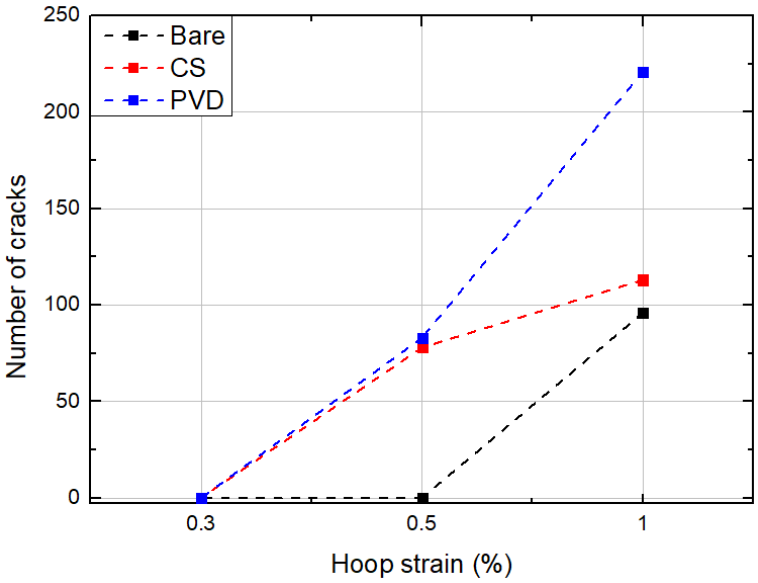


Figure 3: Crack counts after reorientation test for bare, CS and PVD cr-coated cladding. Note that the cracks formed in the bare material were due to hydride fracture at the outer surface of the cladding.

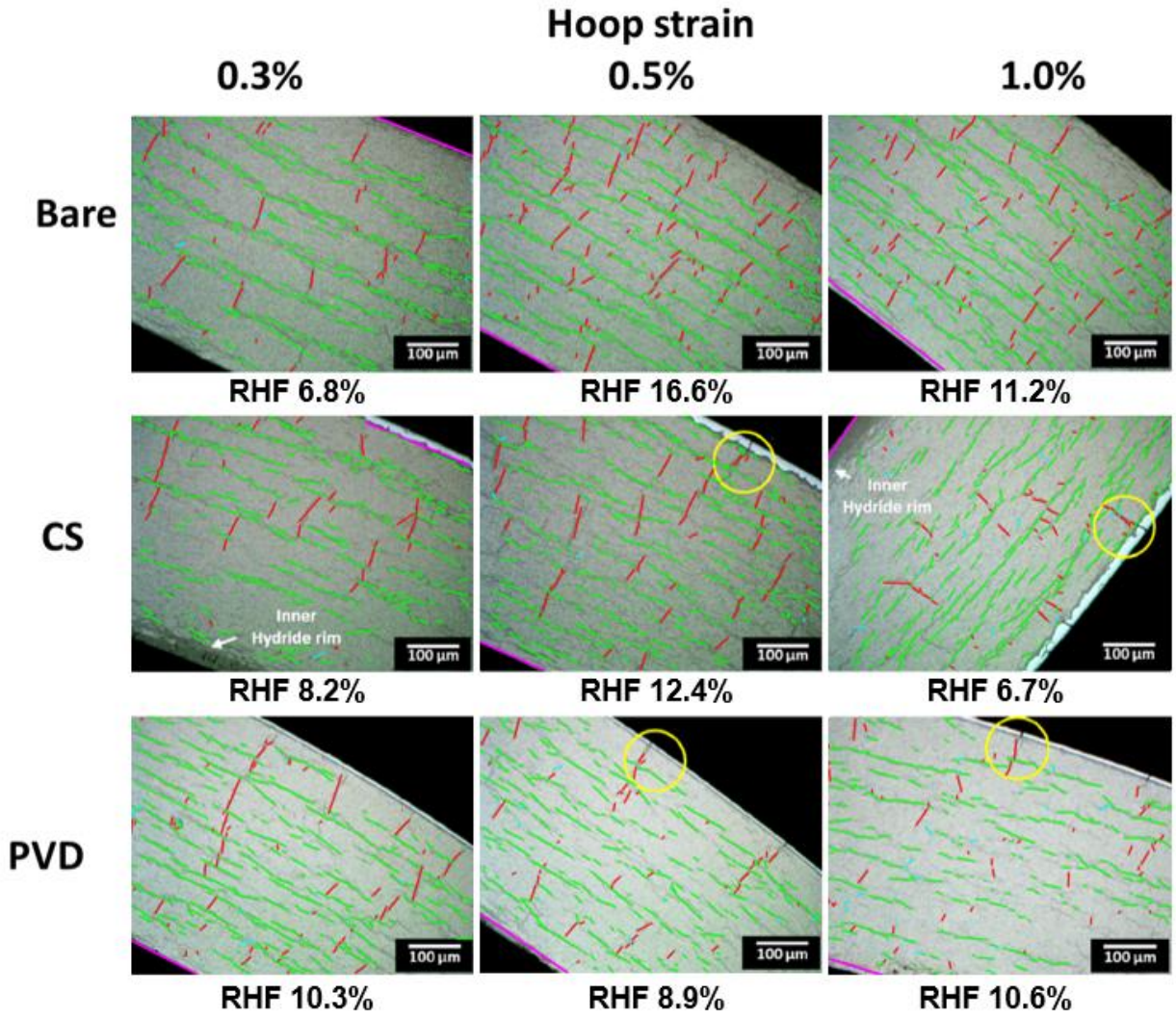


Figure 4: Image analysis results of the radial cross sections presented in Figure 3 using the PROPHET code. Radial hydrides and circumferential hydrides are identified and marked with red and green lines, respectively. The RHF calculated for each specimen is indicated at the bottom of each micrograph.

The uncoated cladding qualitatively displays relatively uniform radial hydride distributions with respect to the radial position, shown using the red-marked radial hydrides in Figure 4. In contrast, the Cr-coated samples exhibit a spatial distribution of radial hydrides that is more concentrated in the outer radial regions while the inner regions of the cladding consist predominantly of circumferential hydrides. These observations suggest that the coating layer may influence the local stress state or hydrogen migration, leading to the localized precipitation of radial hydrides near the outer surface.

5.2 Neutron Radiography

Neutron radiographs showing the full-scale FOV (comprised of two stitched radiographs) and magnified regions of interest are shown in Figure 5 (bare), Figure 6 (CS), and Figure 7 (PVD). A summary of the full-scale FOV collection of all radiographs can be found in Figure 17 of the Supplementary Materials. Circumferential hydrides are clearly visible in all samples, while radial hydrides are more visible in the Cr-coated samples than in the bare cladding. This may appear contradictory to the results shown with optical microscopy in the previous section. While there is still significant radial hydride formation in the bare material, they likely form mis-aligned hydrides in the axial direction of the rod. More specifically, while parallel along the axial direction, they may not align on the same axis. Contrary to the bare cladding, the radial hydrides in the Cr-coated cladding appear to align along the axial direction along the crack tips of the Cr-coating. This likely reflects the highly uniform Cr-coating cracks along the axial direction seen in literature [8, 47]. The axial uniformity of the radial hydrides is important as the radiography shows a two-dimensional average of the 4 mm ring segment. The hydride accumulation around the CS material displays a butterfly shape (highlighted in the 0.5% strain sample) typical of the shear bands that might occur at a crack tip that was also observed within DHC experimentation [15, 42]. The PVD on the other hand have sharper radial precipitation leading from the crack tips.

The inner hydride rim of the 0.3% and 1.0% tests of the CS material is evident within the radiography consistent with optical microscopy. The large saturation of hydrogen at the edge causes difficulty in the hydrogen analysis via image analysis for two reasons. First, the hydrogen standards did not encompass the range of the hydrogen concentrations observed the hydride rims resulting in a less certain calibration with such high hydrogen concentrations. Second, the hydride rim exacerbates the edge effect known to radiography due to the very different neutron scattering cross-sections [48]. This causes greater uncertainty when defining the boundary of the cladding sample for image analysis.

A comparison of the calculated and measured values provided in Table 3 indicates that neutron radiography (from two radiographs, stitched in Figure 5 - Figure 7) predicts the hydrogen concentration relatively well. The error is primarily attributed to the hydride rim effect which is particularly significant for the 0.3% and 1.0% CS specimens. In the case of the 1.0% PVD specimen, the results from the two images used for the calculation are highly consistent, and the actual hydrogen concentration exhibits a very flat profile in the radial direction when averaged over the entire ring. Therefore, the slight discrepancy observed in this case is attributed to a minor hydrogen concentration gradient existing within the specimen itself.

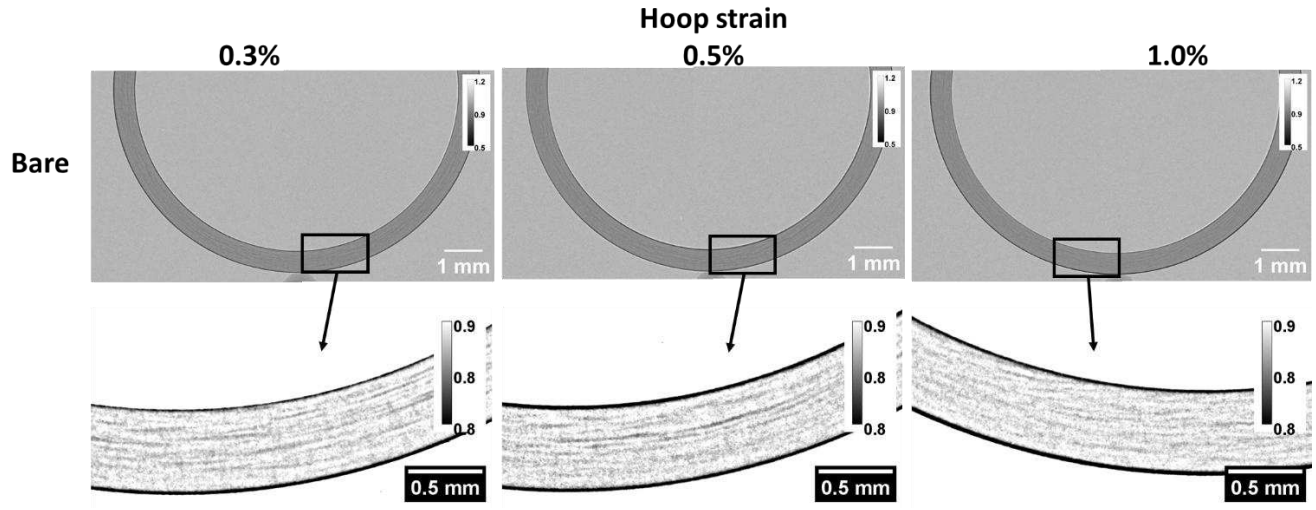


Figure 5: Full view (top) radiographs with magnified views (bottom) of the neutron radiography of the radial cross section from the bare claddings after reorientation testing.

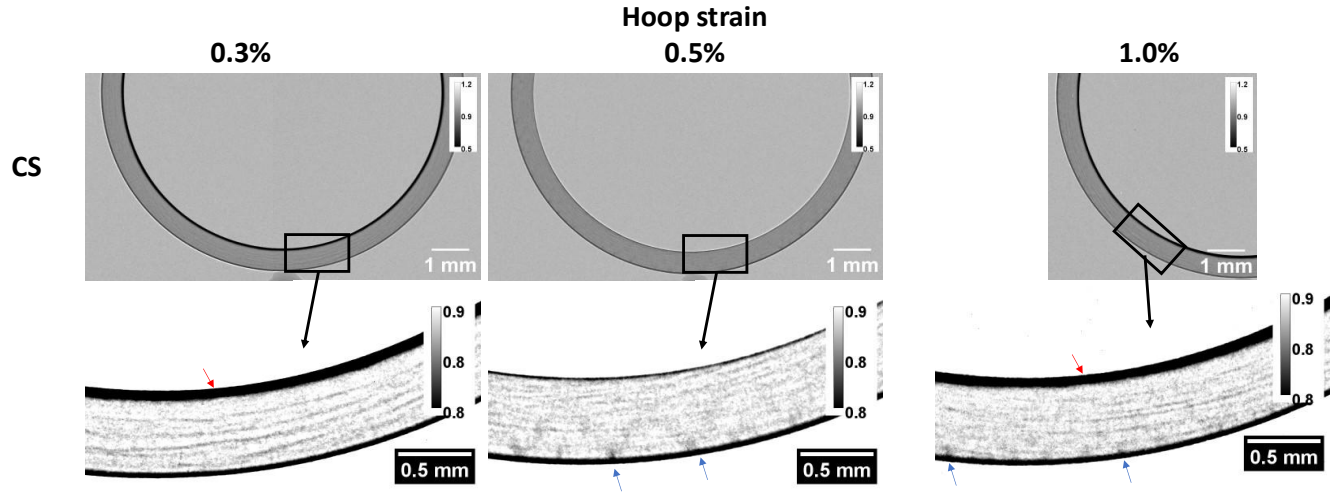


Figure 6: Full view (top) radiographs with magnified views (bottom) of the radial cross section from the CS Cr-coated claddings after reorientation testing. The blue arrows indicate the localized radial hydrides formations near the Cr-coating interface. The red arrows indicate the hydride rim from hydrogen charging.

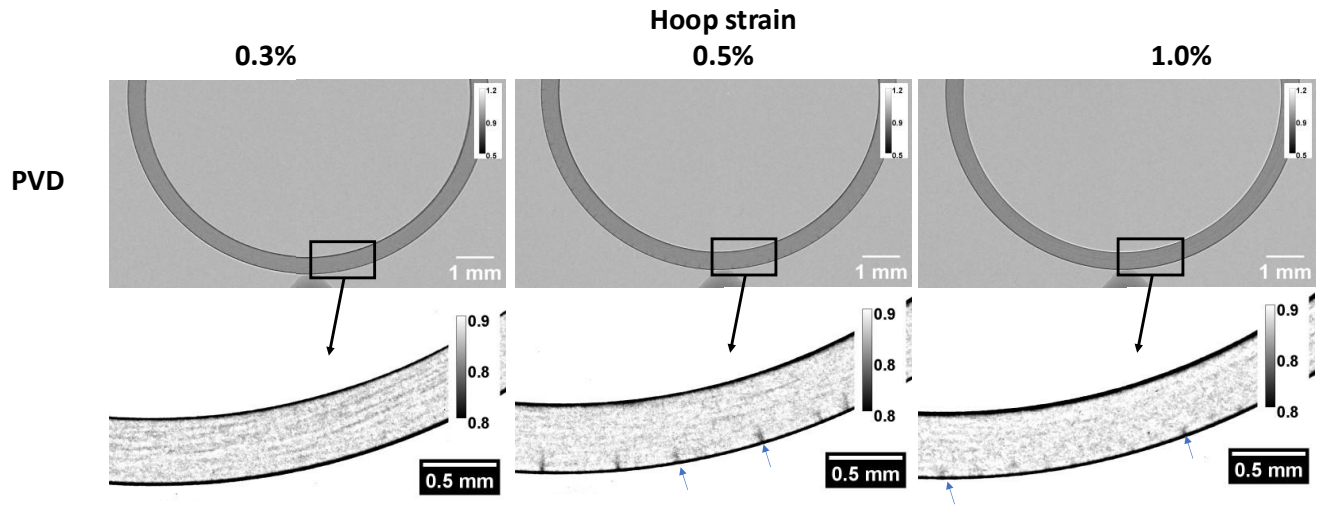


Figure 7: Full view (top) radiographs with magnified views (bottom) of the radial cross section from the PVD Cr-coated claddings after reorientation testing. The blue arrows indicate the localized radial hydrides formations near the Cr-coating interface.

Table 3: Comparison of hydrogen concentrations calculated from NRICH and measured by the hot gas extraction method for each specimen. Two radiographs were captured (left and right side of sample) and used for hydrogen quantification.

		Hydrogen from Radiography			Measured H content (wppm)	Error	
	Strain	Image 1 (wppm)	Image 2 (wppm)	Avg (wppm)		(wppm)	(%)
Bare	0.3	285.76	296.09	**290.9**	**320**	29.1	**9.09**
	0.5	313.49	292.4	**302.9**	**330**	27.1	**8.20**
	1	299.77	286.92	**293.3**	**350**	56.7	**16.2**
CS	0.3	232.97	241.7	**237.3**	**980**	742.7	**75.8**
	0.5	305.41	277.44	**291.4**	**300**	8.6	**2.86**
	1	267.62	-	**267.6**	**960**	692.4	**72.1**
PVD	0.3	336.62	297.36	**317.0**	**310**	7.0	**2.25**
	0.5	297.64	268.74	**283.2**	**370**	86.8	**23.46**
	1	211.11	252.56	**231.8**	**380**	148.2	**38.99**

Further image analysis using the NRICH code provides quantitative hydrogen mapping and radial profiles. Figure 8 though Figure 10 present the local hydride distributions and radial concentration profiles for the bare, CS, and PVD specimens, all at 0.5% hoop strain. The radial profiles in panel (b) of each figure are calculated by averaging 10 pixels along the lines indicated in the radiographs based on the distance from the tube center. Panels (c) and (d) show the raw and smoothed hydride distributions, respectively, with hydride rims removed to preserve the calibrated scale.

In the 0.5% bare case in Figure 8(d), the contour map reveals the morphology of short radial hydrides (marked with black arrows) that are difficult to identify in the raw neutron radiograph of Figure 5. While the average concentration was 320.9 wppm, localized circumferential bands reached significantly higher peak concentrations up to 800 wppm, appearing as intense red regions. The radial profile in Figure 8(b) exhibits periodic peaks where the marked lines intersect these circumferential hydrides. Notably, in the central region of the cladding between 4450 and 4650 μm, the hydrogen concentration shows significant fluctuations while remaining consistently high. This sustained elevation in the profile confirms the presence of radial hydrides within this specific central zone.

In contrast to the more dispersed distribution of the bare cladding, the 0.5% CS case in Figure 9 shows hydrogen concentrated in localized high-intensity regions toward the outer cladding region near the Cr-coating interface. While the overall average concentration was 291.4 wppm, the radial profiles in Figure 9(b) reveal that both Line C and Line D fluctuate between roughly 100 and 600 wppm across the central region and rise toward the outer surface, with peaks approaching ~1000 wppm. This outer-region elevation is consistent with the localized radial hydride formation near the coating cracks observed in the corresponding radiograph (Figure 6).

Similarly, the 0.5% PVD case in Figure 10 shows a distinct morphology despite a similar average concentration of 300 wppm. The hydrogen concentration in radial hydrides at the outer cladding region shown in the radial profile in Figure 10(b) consistently achieves 800 wppm, similar to the outlier datum in Figure 9(b).

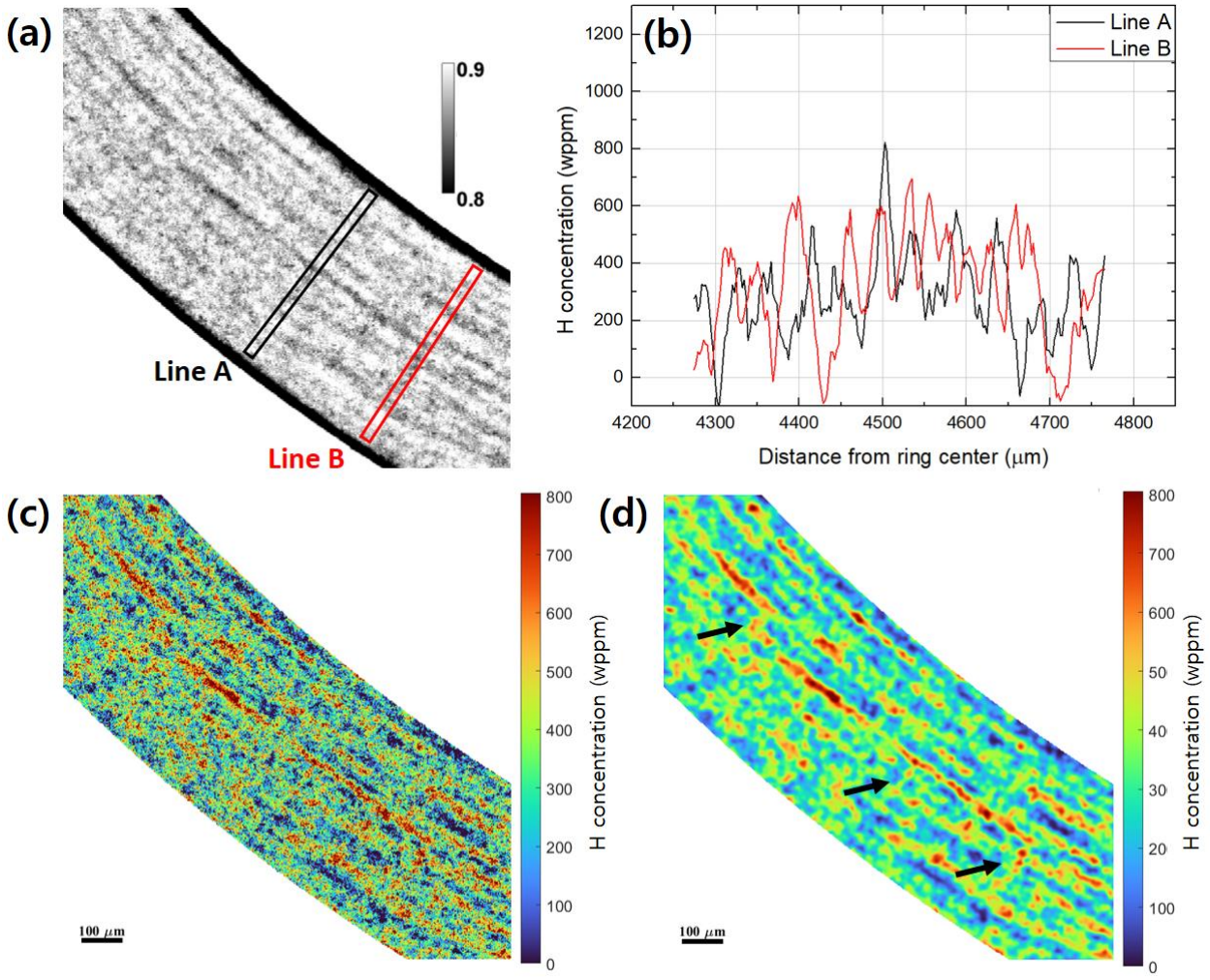


Figure 8: Quantitative hydride characterization for bare Zircaloy-4 cladding at 0.5% hoop strain: (a) cross-sectional radiograph, (b) radial concentration profiles along the lines indicated in (a), (c) raw hydrogen concentration map, and (d) smoothed hydride distribution.

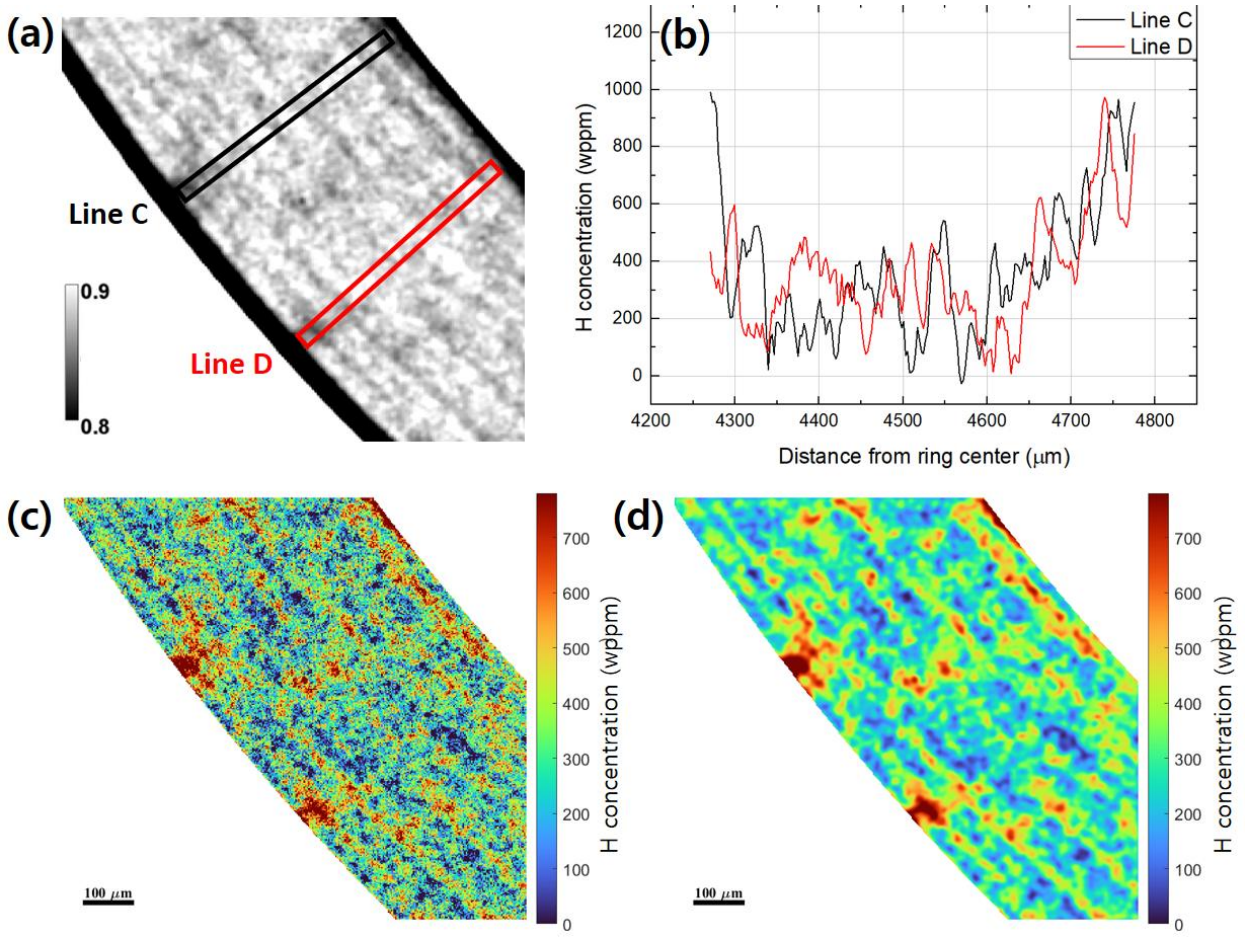


Figure 9: Quantitative hydride characterization for CS Cr-coated cladding at 0.5% hoop strain: (a) cross-sectional radiograph, (b) radial concentration profiles along the lines indicated in (a), (c) raw hydrogen concentration map, and (d) smoothed hydride distribution.

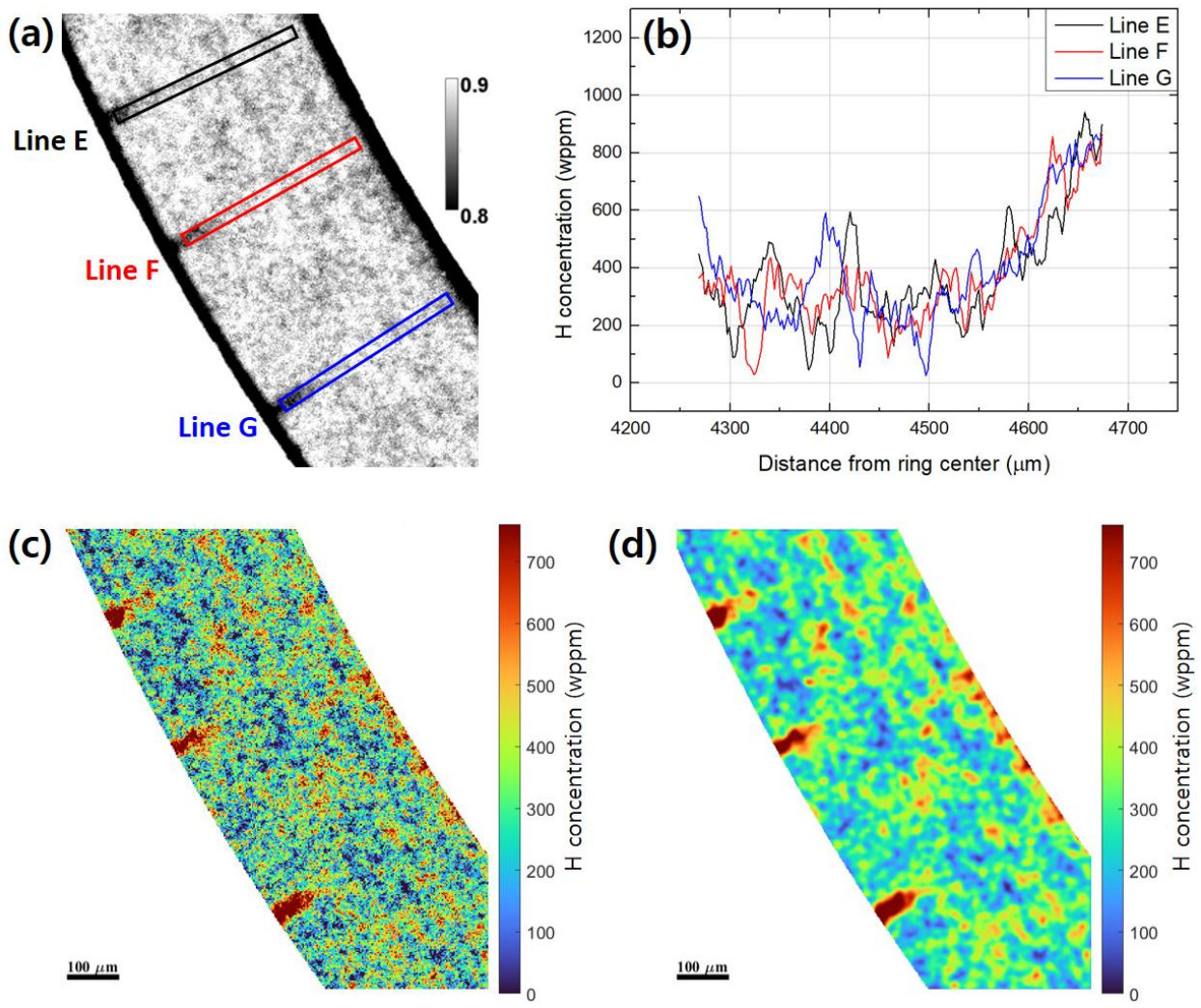


Figure 10: Quantitative hydride characterization for PVD Cr-coated cladding at 0.5% hoop strain: (a) cross-sectional radiograph, (b) radial concentration profiles along the lines indicated in (a), (c) raw hydrogen concentration map, and (d) smoothed hydride distribution.

5.3 Ring Compression Tests

Load versus displacement results from the RCT tests for all tests are shown in Figure 11. The brittle nature of the cladding in all samples after reorientation testing is apparent from the sudden load drop during the test, indicating a crack in the cladding. Several specimens produce multiple load drops and corresponding cracks which are shown with optical microscopy in Figure 12 through Figure 14.

Observations specific to the bare cladding tubes suggest consistency in the material response for all reorientation strain conditions, which display the least amount of yielding prior to cracking and 2-3 significant load drops leading to the end of test. The CS material

showed increased yielding prior to cracking compared to the bare material, higher maximum loads, and higher magnitude of final load drops.

For the PVD tests the maximum load reached was lower due to the thinner wall thickness of the procured cladding (compared to the uncoated and CS cladding material). Nevertheless, the 0.3% and 0.5% strain levels were relatively comparable in response, whereas the 1.0% strain tests showed much longer yielding (0.5 to 1.5 mm versus 3.5 mm) prior to end-of-test. The total yielding prior to failure was much larger than the bare and CS materials. However, the load drops shown in the PVD material appear to be more numerous (more than 2-3 drops) and lower magnitudes (~5-10 N/mm versus ~10-20 N/mm) compared to the bare and CS cladding tubes.

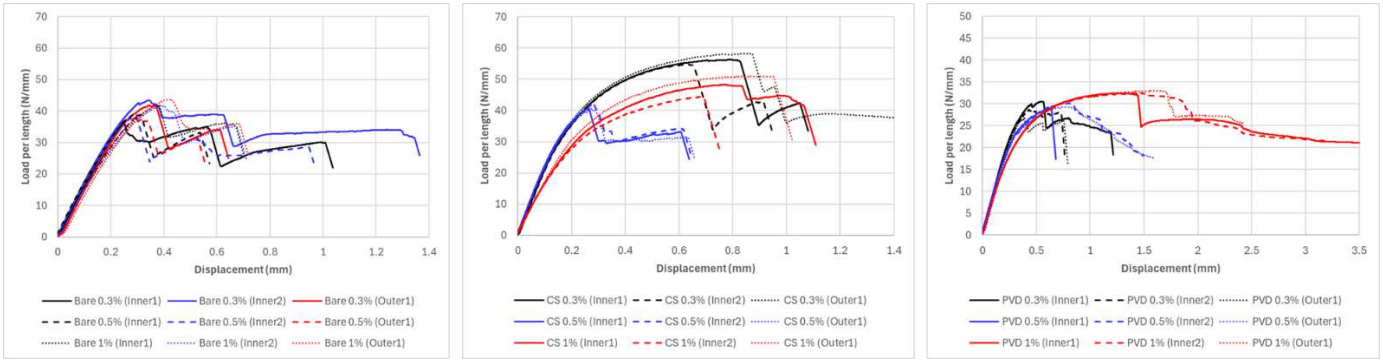


Figure 11: Load versus displacement curves for the RCT testing of the (a) bare cladding, (b) CS Cr-cladding, and (c) PVD Cr-coated cladding.

Figure 12 highlights the crack morphology of the bare cladding tubes after RCT testing. At each azimuthal position that exhibits cracking, only one crack is observed. The cracks can be seen traveling through radially oriented hydrides with connections being made through circumferentially oriented hydrides. In the 0.3% case, the cracks arrest near the opposite cladding at circumferentially oriented hydrides that do not have a near radial hydride. The 0.5% strain case shows the cracks propagate nearly through the cladding wall thickness where potential pathways may be present, i.e. continuous radial hydrides.

Figure 13 presents the crack morphology of select CS cladding tubes after RCT testing. There are many small cracks at the outer diameter of each strain case where radial hydrides form during reorientation testing, particularly at the 3 and 9 o'clock positions. In the 0.3% and 1.0% cases the inner diameter also contains numerous cracks which may result from the hydride rim caused by excessive hydrogen charging. The 0.5% case where no hydride rim is present supports this with only one crack propagating through from the inner surface of the cladding. In the 0.5% and 1.0% case, where coating cracking occurring during reorientation testing, numerous cracks are observed at the outer wall surface which originate at preexisting coating cracks and extend into the Zry-4 where localized radial

hydrides are present. These cracks at the outer wall are much less severe regarding depth of crack when propagating from the outer surface.

Figure 14 presents the crack morphology of select PVD cladding tubes after RCT testing. At lower reorientation strain levels (0.3%), few radial hydrides have from at the coating interface as the coating remained unfractured during reorientation. Similar to the CS cladding tubes at higher reorientation strain levels (0.5% and 1.0%), numerous outer cracks form at pre-existing coating cracks which do not propagate deep into the cladding wall relative to the primary cracks causing failure.

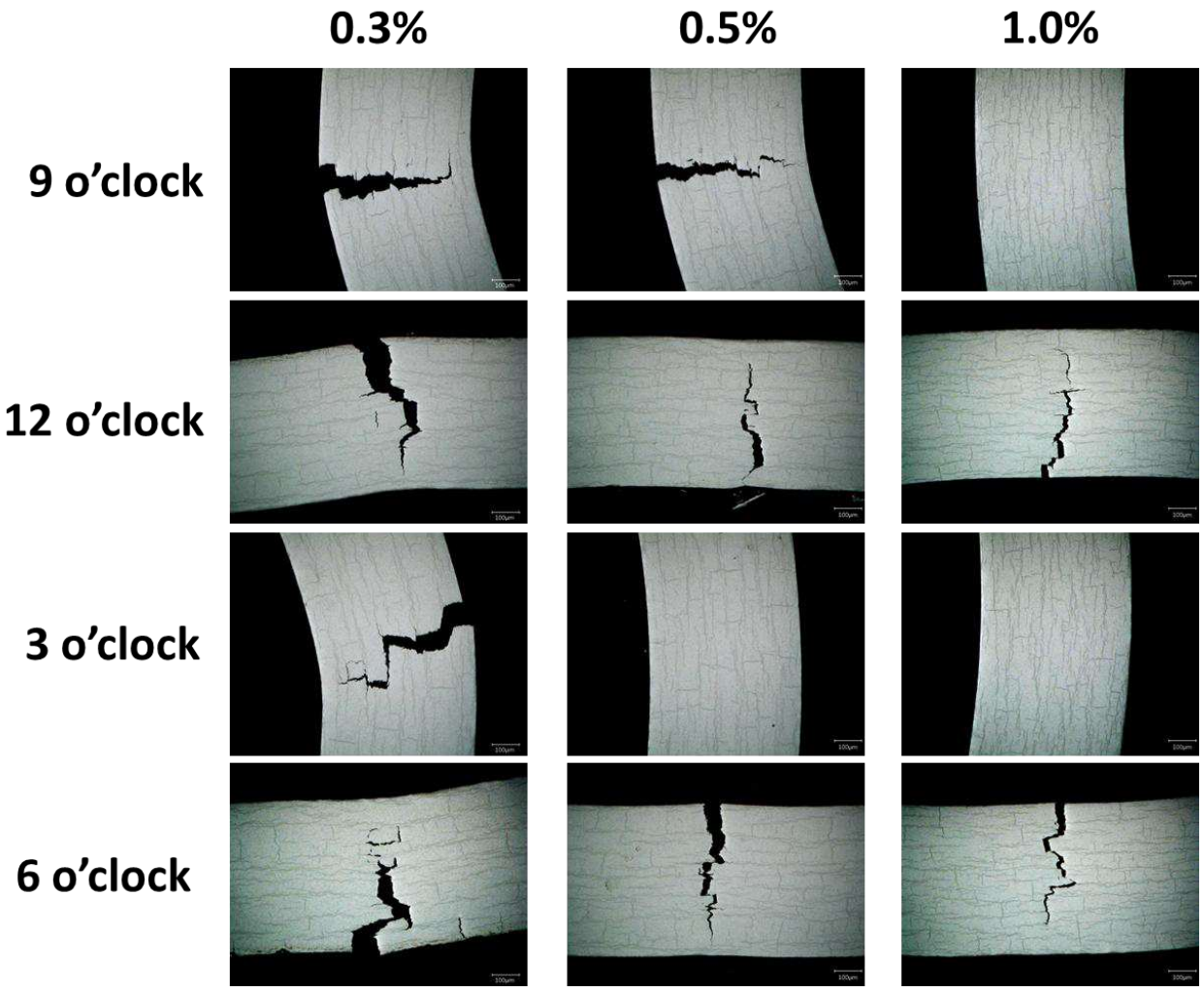


Figure 12: Micrographs of the radial cross section of the bare cladding after RCT testing. The four prominent stress points are highlighted as 9, 12, 3 and 6 o'clock where primary fracture occurred.

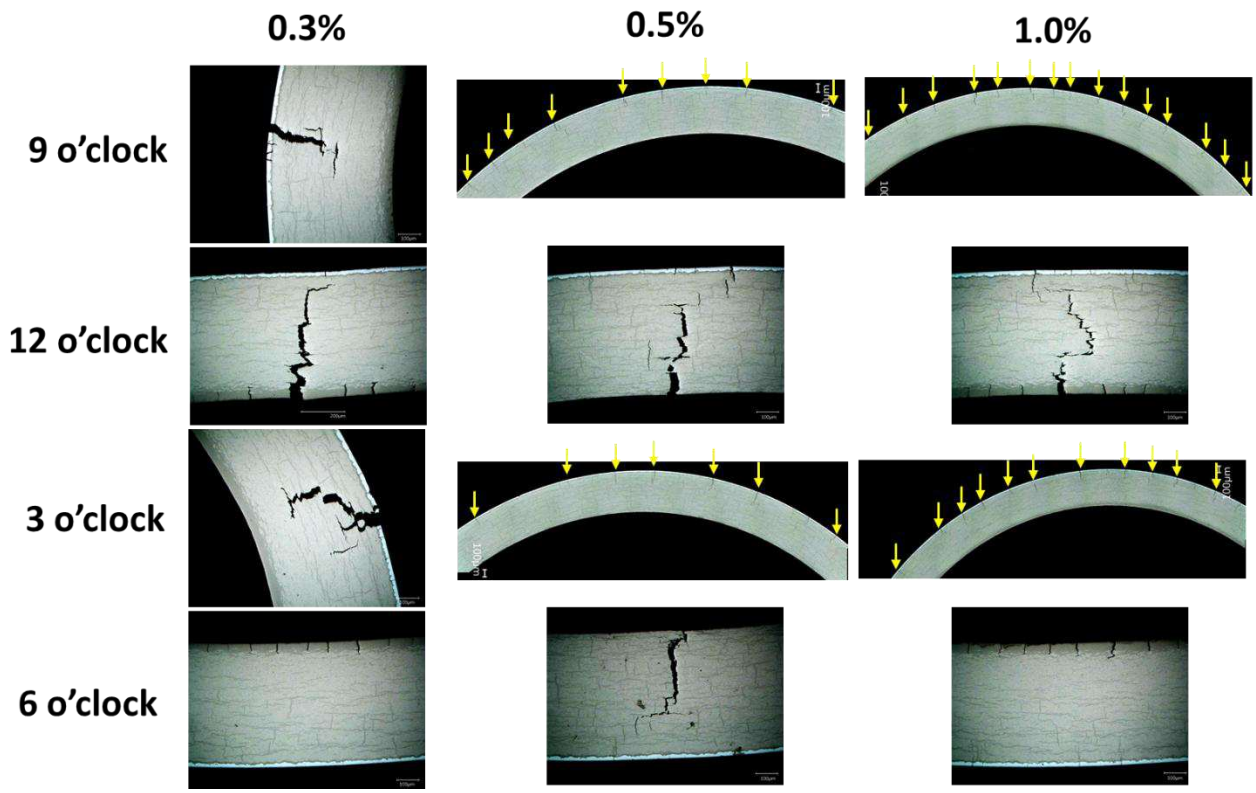


Figure 13: Micrographs of the radial cross section of the CS Cr-coated cladding after RCT testing. The four prominent stress points are highlighted as 9, 12, 3 and 6 o'clock where primary fracture occurred. The 9 and 3 o'clock micrographs have been oriented horizontally for presentation purposes. The yellow arrows highlight the locations of small cracks unique to the deformation in the 9 and 3 o'clock positions.

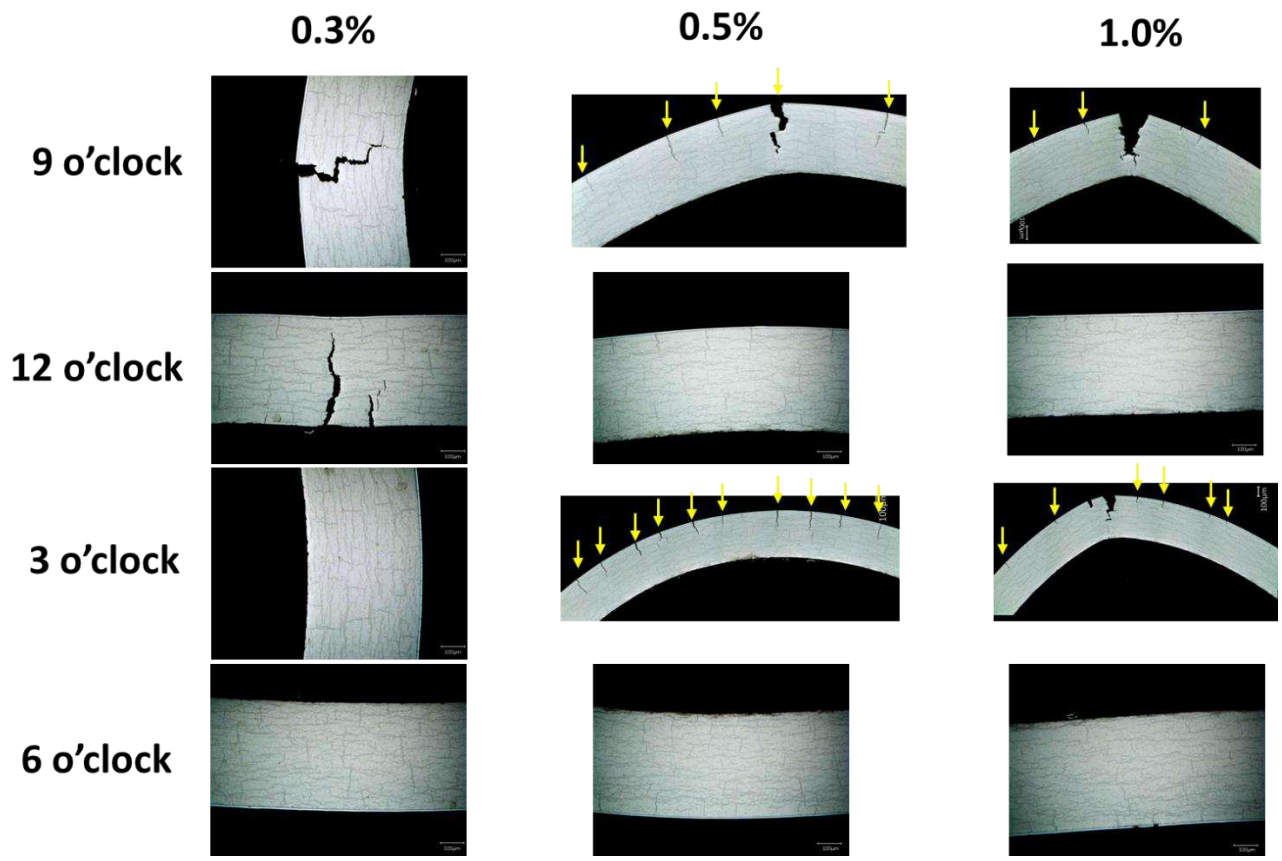


Figure 14: Micrographs of the radial cross section of the PVD Cr-coated cladding after RCT testing. The four prominent stress points are highlighted as 9, 12, 3 and 6 o'clock where primary fracture occurred. The 9 and 3 o'clock micrographs have been oriented horizontally for presentation purposes. The yellow arrows highlight the locations of small cracks unique to the deformation in the 9 and 3 o'clock positions.

6 Discussion

6.1 Coating Effects on Hydride Reorientation

Contrary to the initial expectation that the radial RHF would consistently increase with strain, the total RHF exhibits a more complex behavior. Considering the amount of hydrogen in the material and maximum temperature, it is unlikely that all hydrides underwent dissolution and some remained as circumferential hydrides. For the bare and CS-coated materials, the RHF increased when the strain rose from 0.3% to 0.5%, whereas it decreased at 1.0% strain (Figure 4).

For the 1.0% bare specimen, the lower RHF is attributed to its higher total hydrogen concentration: because the available hydrogen exceeded the amount that could be taken into solution at the peak reorientation temperature (~135 wppm hydrogen [49]), a fraction

of the hydrides did not dissolve and remained as circumferential hydrides upon cooling. This undissolved circumferential population raises the denominator of the radial hydride fraction, lowering the apparent RHF even though radial reorientation still proceeded.

For the 1.0% CS-coated specimen, the thick hydride rim formed at the inner diameter likely suppressed further precipitation of radial hydrides as observed in the optical micrographs. In contrast, the PVD-coated materials maintained a relatively consistent RHF regardless of the applied strain. This insensitivity may be attributed to the thinner (9 μm) PVD coating, which is expected to fracture at a finer and more uniform crack spacing than the thicker (20 μm) cold-spray coating; the resulting crack-tip stress concentrators could be distributed densely enough that the outer-region radial hydride population saturates at low strain and changes little with further straining. The absence of the over-charging-induced inner rim in the PVD specimens also means their RHF was not perturbed by the artifact that lowered the 1.0% CS value.

These variations in RHF and morphology are closely linked to the spatial distribution of the radial hydrides (Figure 4). While the uncoated cladding shows radial hydrides dispersed evenly throughout the entire cladding wall, the Cr-coated cases exhibit a distinct trend where radial hydrides are primarily concentrated in the outer radial regions. In all strain cases, the Cr-coated material exhibits a preference for radial hydrides towards the outer radius near the Cr-coating interface. This pre-cracking bias may be attributed to the mechanical constraint of the stiff, harder Cr coating on the outer surface, which elevates the local tensile stress in the underlying Zry-4 near the coating-cladding interface during reorientation loading and thereby promotes radial hydride precipitation in that region. However, these radial hydrides did not extend directly from the coating at strain levels below the cracking threshold observed between 0.3% and 0.5% hoop strain. Once the coating fractured above 0.3% hoop strain, radial hydrides were distinctly focused at each of the coating crack tips. This localized accumulation strongly indicates that stress concentrations caused by coating cracking dictate the hydride precipitation pattern.

It is noteworthy that the CS specimens in the 0.3% and 1.0% strain cases had elevated hydrogen concentrations, leading to an inner hydride rim. This rim is considered a specimen artifact resulting from over-charging during the hydrogen loading process. While this was an undesired condition, it likely did not affect the reorientation tests as the stress state at the outer region remained minimally impacted. It should be emphasized that the inner-diameter rim and the radial-hydride reorientation occur in spatially distinct regions: the over-charging artifact is confined to the inner surface, whereas the stress-driven reorientation of interest occurs near the outer coating interface. Consequently, although the rim lowers the measured radial hydride fraction by occupying the inner wall with

circumferential hydrides, it does not alter the outer-region reorientation behavior that is the focus of this work. Similar observations are made in the PVD-coated materials: radial hydrides formed at each coating crack due to local stress concentrations. However, prior to the onset of coating cracking, radial hydrides in PVD samples formed up to the outer interface of the coating. The crack counts in the Cr-coating for each sample (Figure 4) confirm that crack onset occurs between 0.3% and 0.5% hoop strain, consistent with previously reported findings [6, 8, 50] [23].

6.2 Radiography as Hydrogen Quantification

NRICH analysis produced bulk hydrogen concentrations in reasonable agreement with the destructive hot gas extraction measurements (Table 3), particularly where hydride rims are not present, demonstrating that the hydrogen concentration can be quantified with this method for claddings subjected to complex heat treatments. Radiography highlights the advantage over classical image analysis (quantifying hydrogen though phase fraction) of optical micrographs which are subject to sample preparation and sample heat treatments. Hydrogen quantification and visualization though neutron radiography is not subject to sample preparation or heat treatment. Specifically, the radiograph is a result of physical interactions with the oncoming neutron and hydrogen atoms within the sample.

In this work the NRICH GUI was calibrated with samples of hydrogen content lower than what was measured in the hydride rim of some of the samples. While the calibration curve is largely linear, the range is not captured and likely introduces some error. Additionally, the samples that were destructively measured with hot gas vacuum extraction were not directly analyzed with neutron radiography (see cutting diagram in Figure 15). Rather, the samples destructively examined with hot gas extraction were rather adjacent to the samples subjected to radiography. While it was assumed that the hydrogen contents should be very similar, the complex heat treatment through hydrogen charging and reorientation testing may have caused some axial and radial variation in the hydrogen content introducing some errors in the comparison of hydrogen concentrations.

6.3 Coated Cladding Reorientation Effects on Mechanical Response

RCT testing highlights the change in the mechanical response of the Cr-coated claddings compared to bare material. The bare material exhibited a typical mechanical response to hydride reorientation where the primary fracture pathways are found at angular-dependent points of failure. The load versus displacement highlights abrupt load drops indicating significant displacement from the single points of failure. These observations indicate a high connectivity of the hydride throughout the wall thickness making it more vulnerable to

a through thickness failure. The 1.0% case showed the least cracking but may be subject to the cross-section of the sample polished, creating a misleading perspective of crack morphology.

The CS materials displayed more focused hydride reorientation at the coating-cladding interface that led to a higher number of crack initiation points. This appears to lead to an increased overall yield before failure due to the increased number of points available to accommodate deformation. Additionally, the radial hydrides are focused on the outer half of the cladding, as highlighted with radiography, resulting in a discontinuity of radial hydrides to the inner surface. The discontinuous nature of the radial hydrides is beneficial for through wall fracture as the fracture pathway will be arrested in the ductile Zry-4 base matrix sooner or redirected along circumferential hydrides. This is evident when comparing the general fracture depth and opening of the bare material with CS material.

The PVD coated cladding tubes display increased ductility before cracking with increased reorientation test strain levels. This presents a somewhat counterintuitive trend where the macroscopic ductility and the number of outer cracks follow inverse trends with respect to the reorientation strain. This observation supports that the presence of localized preexisting cracks in the coating helps accommodate initial deformation (see Figure 3) distributing the strain which allows the entire specimen to deform more before brittle failure (outside axis limit of Figure 14). The maximum loads observed in the PVD samples are lower than the CS samples as result from the thinner walled Zry-4 cladding in addition to different specifications compared the base Zry-4 from the bare and CS samples. Notably, the PVD 1.0% specimen contains significantly fewer and shorter radial hydrides compared to the lower strain cases. The preexisting coating cracks in these high strain specimens act as strain accommodators effectively absorbing localized deformation. This is supported by the absence of small secondary cracks in the PVD 0.3% specimen which lacked such strain relieving preexisting cracks and thus failed more abruptly. To avoid ambiguity, two crack populations should be distinguished: 1) coating cracks introduced during reorientation testing, present before ring compression and acting as preexisting strain-accommodation sites, and 2) through-wall cracks that initiate during the RCT. The enhanced ductility of both Cr-coated materials arises from population 1): a larger number of preexisting coating cracks distributes deformation over more sites and delays the formation of a single dominant through-wall pathway. The apparent inverse relationship in the PVD specimens — greater ductility despite fewer RCT-induced cracks at higher reorientation strain — is therefore consistent rather than contradictory, since the higher reorientation strain generated more preexisting coating cracks that accommodated deformation and suppressed new crack initiation.

Overall, the greater number of coating cracks in the Cr-coated materials acted as distributed strain relief sites, reducing the likelihood of a single catastrophic failure pathway. This crack-mediated redistribution of deformation contributed to the enhanced ductility observed in both CS and PVD specimens during RCT testing.

Taken together, the microstructural and mechanical observations can be linked through the spatial distribution of the radial hydrides. In the bare cladding, radial hydrides span the full wall thickness, forming a well-connected network that provides a direct through-wall fracture pathway and the abrupt, single-pathway failures seen in the RCT. In both Cr-coated materials, radial hydrides are instead confined to the outer region and remain discontinuous toward the inner wall, so fracture initiating at the outer cracks is arrested or deflected within the ductile Zry-4 matrix, producing the higher ductility and distributed cracking observed mechanically. This coupling between hydride distribution and fracture response indicates that the Cr coating enhances the residual ductility of reoriented, hydrided cladding by localizing radial hydrides away from a continuous through-wall path — a behavior directly relevant to maintaining cladding integrity under the slow-cooling and handling stresses of spent-fuel dry storage.

7 Conclusion

Through hydride reorientation testing of bare, CS, and PVD Cr-coated cladding tubes, a distinct hydride reorientation response occurs with the presence of a Cr-coating. In the presence of a Cr-coating hydride reorientation was focused on locations of coating cracks due to the local stress concentrations. Additionally, the outer diameter of the Cr-coated claddings showed most of the reorientation due to the increased number of local stress concentrations caused by the cracking. Furthermore, the NRICH application demonstrated and provided quantitative confirmation of the local and average hydrogen concentrations of samples that underwent complicated hydrogen charging and thermal treatment offering a more resolved understanding of the distribution of reoriented hydrides. RCT testing demonstrated the mechanical response of Cr-coated cladding with reoriented hydrides responded differently than bare cladding due to the increased number radially oriented hydrides at the outer surface. Specifically, a higher number of fracture points occurred at the surface reoriented hydrides leading to more regions for yielding. Further investigations can be performed to quantify with greater statistical certainty the effects of a Cr-coating on hydride reorientation.

8 Acknowledgments

We would like to thank Alex Pomo for support with internal pressurization testing and metallography preparations and David Cottle for support with hydrogen charging.

9 Funding

This work was supported by the U.S. Department of Energy through the Advanced Fuels Campaign.

10 References

[1] I. A. E. Agency, "Nuclear Power Reactors In The World," 2025.

[2] J.-C. Brachet *et al.*, "Some practical methodologies to assess the overall high temperature (one-sided) steam oxidation protectiveness of chromium-based coatings on a zirconium-based substrate, as Enhanced – Accident tolerant (Nuclear) fuels (E-ATF) claddings," *Journal of Nuclear Materials,* vol. 606, p. 155620, 2025/02/01/ 2025, doi: https://doi.org/10.1016/j.jnucmat.2025.155620.

[3] K. A. Terrani, "Accident tolerant fuel cladding development: Promise, status, and challenges," in *Journal of Nuclear Materials* vol. 501, ed: Elsevier B.V., 2018, pp. 13-30.

[4] C. Tang, M. Stueber, H. J. Seifert, and M. Steinbrueck, "Protective coatings on zirconium-based alloys as accident-Tolerant fuel (ATF) claddings," *Corrosion Reviews,* vol. 35, no. 3, pp. 141-165, 2017/8// 2017, doi: 10.1515/corrrev-2017-0010.

[5] J. Yang *et al.*, "Review on chromium coated zirconium alloy accident tolerant fuel cladding," *Journal of Alloys and Compounds,* vol. 895, 2022/2// 2022, doi: 10.1016/j.jallcom.2021.162450.

[6] I. Alakiozidis *et al.*, "Quantifying cracking and strain localisation in a cold spray chromium coating on a zirconium alloy substrate under tensile loading at room temperature," *Journal of Nuclear Materials,* vol. 591, 2024, doi: 10.1016/j.jnucmat.2024.154899.

[7] I. Alakiozidis *et al.*, "Semi-integral LOCA testing of Cr-coated Optimized ZIRLOTM claddings," *Journal of Nuclear Materials,* vol. 610, p. 155766, 2025/05/01/ 2025, doi: https://doi.org/10.1016/j.jnucmat.2025.155766.

[8] D. V. Nguyen *et al.*, "Mechanical behavior of a chromium coating on a zirconium alloy substrate at room temperature," *Journal of Nuclear Materials,* vol. 558, 2022/1// 2022, doi: 10.1016/j.jnucmat.2021.153332.

[9] C. Dunbar, W. Jung, R. Armstrong, K. Sridharan, M. Corradini, and H. Yeom, "Fuel performance analysis of Cr-coated Zircaloy-4 cladding during a prototypical LOCA event using BISON," *Annals of Nuclear Energy,* vol. 200, p. 110411, 2024/06/01/ 2024, doi: https://doi.org/10.1016/j.anucene.2024.110411.

[10] S. B. Bell, T. Graening, A. Evans, P. Kelly, B. A. Pint, and K. A. Kane, "Burst and oxidation behavior of Cr-coated Zirlo during simulated LOCA testing," *Journal of Nuclear Materials,* vol. 564, p. 153679, 2022/06/01/ 2022, doi: https://doi.org/10.1016/j.jnucmat.2022.153679.

[11] R. Sweet, P. Mouche, S. Bell, K. Kane, and N. Capps, "Chromium-coated cladding analysis under simulated LOCA burst conditions," *Annals of Nuclear Energy,* vol. 176, p. 109275, 2022/10/01/ 2022, doi: https://doi.org/10.1016/j.anucene.2022.109275.

[12] K. Kane *et al.*, "The response of accident tolerant fuel cladding to LOCA burst testing: A comparative study of leading concepts," *Journal of Nuclear Materials,* vol. 574, p. 154152, 2023/02/01/ 2023, doi: https://doi.org/10.1016/j.jnucmat.2022.154152.

[13] N. A. P. Kiran Kumar, J. A. Szpunar, and Z. He, "Preferential precipitation of hydrides in textured zircaloy-4 sheets," *Journal of Nuclear Materials,* vol. 403, no. 1, pp. 101-107, 2010/08/01/ 2010, doi: https://doi.org/10.1016/j.jnucmat.2010.06.005.
[14] E. Tenckhoff, "Deformation Mechanisms, Texture and Anisotropy in," *Zirconium and Zircaloy,* vol. STP 966, 1988.
[15] A. W. Colldeweih, "Delayed Hydride Cracking in Irradiated and Unirradiated Zircaloy-2 Cladding," ed, 2022, pp. 1-187.
[16] A. W. Colldeweih, F. Fagnoni, P. Trtik, R. Zubler, M. A. Pouchon, and J. Bertsch, "Delayed hydride cracking in Zircaloy-2 with and without liner at various temperatures investigated by high-resolution neutron radiography," *Journal of Nuclear Materials,* vol. 561, pp. 153549-153549, 2022, doi: 10.1016/j.jnucmat.2022.153549.
[17] A. Colldeweih and J. Bertsch, "Effect of Temperature and Hydrogen Concentration on the Threshold Stress Intensity Factor of Radial Delayed Hydride Cracking in Fuel Cladding," *Journal of Nuclear Materials,* vol. 565, pp. 153737-153737, 2022, doi: 10.1016/j.jnucmat.2022.153737.
[18] Y.-J. Jia and W.-Z. Han, "Effect of external stress on hydride reorientation in zirconium," *Acta Materialia,* vol. 235, p. 118100, 2022/08/15/ 2022, doi: https://doi.org/10.1016/j.actamat.2022.118100.
[19] M. N. Cinbiz, D. A. Koss, and A. T. Motta, "The influence of stress state on the reorientation of hydrides in a zirconium alloy," *Journal of Nuclear Materials,* vol. 477, pp. 157-164, 2016/08/15/ 2016, doi: https://doi.org/10.1016/j.jnucmat.2016.05.013.
[20] A. W. Colldeweih and M. R. M. M. Nelson, N. Capps, P. Trtik, W. H. Jung, and D. W. Kamerman, "Initial Characterizations of Cr-Coated Cladding after Load-Following and Accident Scenario," *Zirconium in the Nuclear Industry: 21st International Symposium,* vol. ASTM International, 2026, 2026, doi: http://doi.org/10.1520/STP166020250035.
[21] A. W. Colldeweih *et al.*, "Cr-coated Zircaloy-4 Performance During Ramping Conditions," in *Proceedings of the 12th World Conference on Neutron Radiography*, Cham, A. E. Craft and H. Z. Bilheux, Eds., 2026// 2026: Springer Nature Switzerland, pp. 32-39.
[22] D. Geng *et al.*, "Hoop expansion deformation and cracking behavior of Cr-coated Zr cladding at 320 ℃: A comparative study before and after hydrothermal corrosion," *Journal of Nuclear Materials,* vol. 619, p. 156285, 2026/01/01/ 2026, doi: https://doi.org/10.1016/j.jnucmat.2025.156285.
[23] A. Colldeweih, Kamerman D., Nelson, M., Craft, A., Capps, N., Massey, C., Ridley, M., Trtik, P., Meyer, M., Yetik O., "Cr-coated Zircaloy-4 performance during ramping conditions," in *WCNR-12*, Idaho Falls, USA, 2024: Springer Nature.
[24] W. Gong *et al.*, "Hydrogen diffusion and precipitation in duplex zirconium nuclear fuel cladding quantified by high-resolution neutron imaging," *Journal of Nuclear Materials,* vol. 526, pp. 151757-151757, 2019, doi: 10.1016/j.jnucmat.2019.151757.
[25] D. Kim, D. Woo, and Y. Lee, "Radial hydride fraction with various rod internal pressures and hydrogen contents for Zr-Nb alloy cladding tube," *Journal of Nuclear*

Materials, vol. 572, p. 154036, 2022/12/15/ 2022, doi: https://doi.org/10.1016/j.jnucmat.2022.154036.
[26] D. Woo and Y. Lee, "Understanding the mechanical integrity of Zircaloy cladding with various radial and circumferential hydride morphologies via image analysis," *Journal of Nuclear Materials,* vol. 584, p. 154560, 2023/10/01/ 2023, doi: https://doi.org/10.1016/j.jnucmat.2023.154560.
[27] J. Ruiz-Hervias, K. Simbruner, M. Cristobal-Beneyto, D. Perez-Gallego, and U. Zencker, "Failure mechanisms in unirradiated ZIRLO® cladding with radial hydrides," *Journal of Nuclear Materials,* vol. 544, p. 152668, 2021/02/01/ 2021, doi: https://doi.org/10.1016/j.jnucmat.2020.152668.
[28] *Standard Specification for Wrought Zirconium and Zirconium Alloy Seamless and Welded Tubes for Nuclear Service*, ASTM B353-12, 2022.
[29] A. Fazi, M. Sattari, K. Stiller, H.-O. Andrén, and M. Thuvander, "Performance and evolution of cold spray Cr-coated optimized ZIRLO™ claddings under simulated loss-of-coolant accident conditions," *Journal of Nuclear Materials,* vol. 576, p. 154268, 2023/04/01/ 2023, doi: 10.1016/j.jnucmat.2023.154268.
[30] H. Yeom and K. Sridharan, "Cold spray technology in nuclear energy applications: A review of recent advances," *Annals of Nuclear Energy,* vol. 150, p. 107835, 2021/01/01/ 2021, doi: 10.1016/j.anucene.2020.107835.
[31] C. P. M. T. Graening, K. Linton, A. Nelson, "Microstructure Investigation and Mechanical Properties of Coated Zircaloy Cladding," ORNL/SPR-2021/2038, 2021.
[32] M. R. T. Graening, J. Werden, K. Linton, N. Capps, "Impact of Flawed Coatings on the Microstructure under Relevant Operating Conditions," ORNL/SPR-2023/2992, 2023.
[33] R. V. Umretiya *et al.*, "Hydrothermal corrosion of PVD and cold spray Cr-coatings on Zircaloy-4 in hydrogenated and oxygenated LWR coolant environments," *Nuclear Materials and Energy,* vol. 37, 2023, doi: 10.1016/j.nme.2023.101519.
[34] J. C. Brachet *et al.*, "Evaluation of Equivalent Cladding Reacted parameters of Cr-coated claddings oxidized in steam at 1200 °C in relation with oxygen diffusion/partitioning and post-quench ductility," *Journal of Nuclear Materials,* vol. 533, 2020/5// 2020, doi: 10.1016/j.jnucmat.2020.152106.
[35] C. D. J. Bischoff, N. Chaari, C. Vauglin, K. Buchanan, et al., "Cr-coated cladding development at Framatome," presented at the Top Fuel 2018, Prague, Czech Republic, 2018.
[36] S. B. Bell, M. J. Ridley, C. P. Massey, and N. A. Capps, "Step-loaded creep testing of Zircaloy-4 cladding at higher temperatures in the α-phase," *Acta Materialia,* vol. 288, 2025, doi: 10.1016/j.actamat.2025.120821.
[37] D. Kamerman, M. Bachhav, T. Yao, X. Pu, and J. Burns, "Formation and characterization of hydride rim structures in Zircaloy-4 nuclear fuel cladding tubes," *Journal of Nuclear Materials,* vol. 586, 2023, doi: 10.1016/j.jnucmat.2023.154675.
[38] M. Nelson, S. Samuha, D. Kamerman, and P. Hosemann, "Temperature-Dependent Mechanical Anisotropy in Textured Zircaloy Cladding," *Journal of Nuclear Materials,* vol. 595, 2024, doi: 10.1016/j.jnucmat.2024.155045.
[39] U. S. NRC, "Standard Review Plan - NUREG-0800," 2007.

[40] W. Gong, P. Trtik, S. Valance, and J. Bertsch, "Hydrogen diffusion under stress in Zircaloy: High-resolution neutron radiography and finite element modeling," *Journal of Nuclear Materials,* vol. 508, pp. 459-464, 2018, doi: 10.1016/j.jnucmat.2018.05.079.

[41] W. Gong, P. Trtik, F. Ma, Y. Jia, J. Li, and J. Bertsch, "Hydrogen diffusion and precipitation under non-uniform stress in duplex zirconium nuclear fuel cladding investigated by high-resolution neutron imaging Weijia," *Journal of Nuclear Materials,* vol. 570, pp. 153971-153971, 2022, doi: /10.1016/j.jnucmat.2022.153971.

[42] A. W. Colldeweih *et al.*, "Radial Delayed Hydride Cracking in Irradiated Zircaloy-2 Cladding: Advanced Characterization Techniques," in *Zirconium in the Nuclear Industry: 20th International Symposium, ASTM STP1645*, Ottowa, ON, M. Preuss, Ed., 2022: ASTM.

[43] P. Trtik and E. H. Lehmann, "Progress in High-resolution Neutron Imaging at the Paul Scherrer Institut-The Neutron Microscope Project," *Journal of Physics: Conference Series,* vol. 746, no. 1, pp. 0-6, 2016, doi: 10.1088/1742-6596/746/1/012004.

[44] A. P. Kaestner *et al.*, "The ICON beamline – A facility for cold neutron imaging at SINQ," *Nuclear Instruments and Methods in Physics Research Section A: Accelerators, Spectrometers, Detectors and Associated Equipment,* vol. 659, no. 1, pp. 387-393, 2011/12/11/ 2011, doi: https://doi.org/10.1016/j.nima.2011.08.022.

[45] B. Blau *et al.*, "The Swiss Spallation Neutron Source SINQ at Paul Scherrer Institut," *Neutron News,* vol. 20, no. 3, pp. 5-8, 2009/08/03 2009, doi: 10.1080/10448630903120387.

[46] D. Kim, D. Kim, D. Woo, and Y. Lee, "Development of an image analysis code for hydrided Zircaloy using Dijkstra's algorithm and sensitivity analysis of radial hydride continuous path," *Journal of Nuclear Materials,* vol. 564, p. 153647, 2022/06/01/ 2022, doi: https://doi.org/10.1016/j.jnucmat.2022.153647.

[47] A. W. Colldeweih. *Post Ramp and LOCA Simulation characterization of Cr-coated Zircaloy-4*.

[48] E. Lehmann, M. Schulz, Y. Wang, and A. Tartaglione, "Edge Enhancement Investigations by Means of Experiments and Simulations," *Physics Procedia,* vol. 88, no. September 2016, pp. 282-289, 2017, doi: 10.1016/j.phpro.2017.06.039.

[49] B. F. Kammenzind, D. G. Franklin, H. R. Peters, and W. J. Duffin, "Hydrogen pickup and redistribution in alpha-annealed Zircaloy-4," *ASTM Special Technical Publication,* vol. 1295, pp. 338-370, 1996, doi: 10.1520/stp16180s.

[50] J. Jiang *et al.*, "Temperature-dependent deformation and cracking behavior in Cr coating for accident tolerant fuel cladding: An in situ SEM study," *Surface and Coatings Technology,* vol. 427, p. 127815, 2021/12/15/ 2021, doi: https://doi.org/10.1016/j.surfcoat.2021.127815.

11 Supplementary Materials

11.1 Specimen Preparation

Following the reorientation tests the tubes are systematically cut samples into specimen segments for various characterization techniques including optical microscopy, neutron radiography, hydrogen analysis, and ring compression testing. Figure 15 describes the locations for each of the segments with the respective length for each of the specimen. Specimens for optical microscopy were etched using methods described in [33].

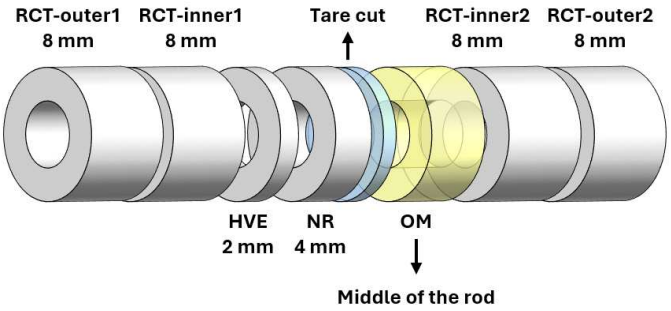


Figure 15: Cutting diagram of the tubes following hydrogen charging and reorientation testing showing the location of the optical microscopy, neutron radiography, hydrogen analysis, and ring compression segments.

11.2 As-charged materials.

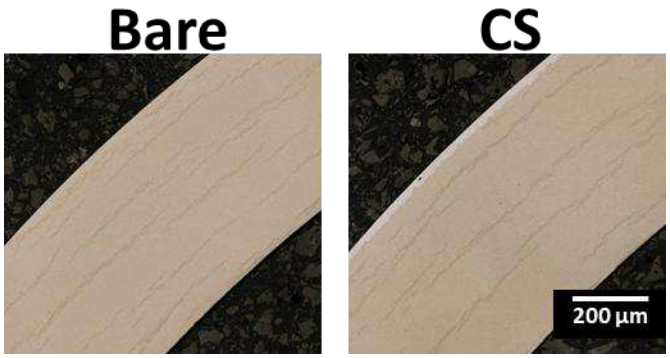


Figure 16: As-charged materials from the bare and CS cladding tubes. The charging process was identical for all tubes. The images are representative of the as-charged state.

11.3 Full-Scale FOV Neutron Radiographs

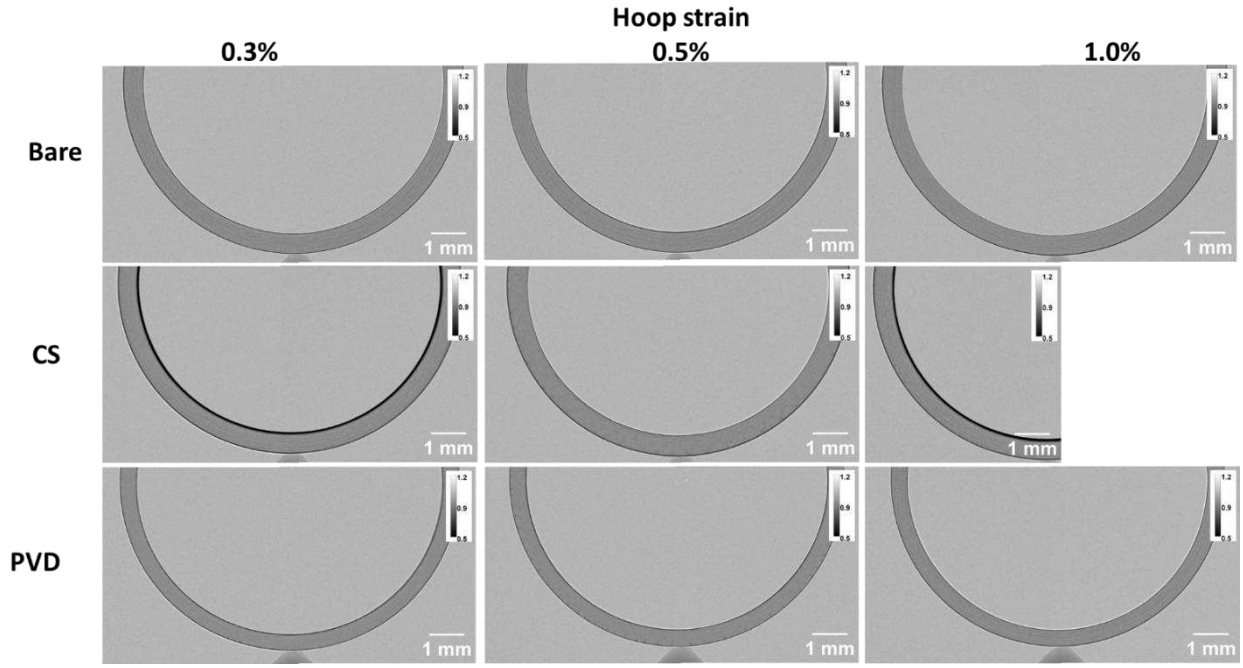


Figure 17: Full-scale FOV neutron radiographs comprised of two stitched radiographs.

11.4 RCT testing parameters and explanations

For each condition in the test matrix (Table 2), three ring specimens were tested to evaluate the consistency of the mechanical response. The three specimens are labeled inner 1, inner 2, and outer according to their extraction position along the parent tube; these designations are used to identify the individual load–displacement curves presented in the Results section, and the corresponding extraction locations are provided in the Supplementary Materials (Section 9.1).

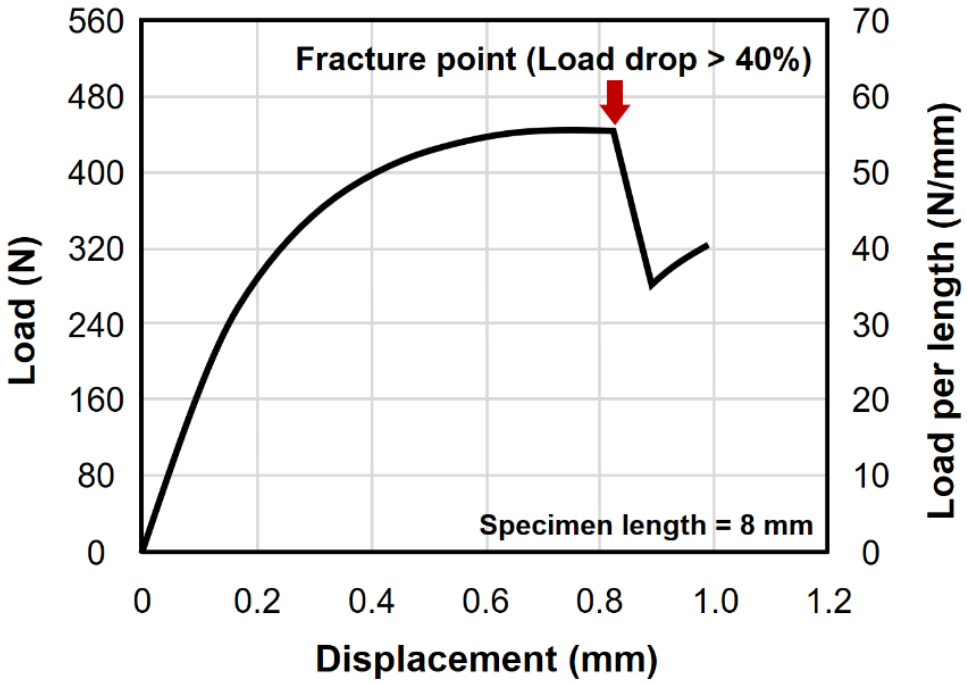


Figure 18: Exemplary load-displacement curve obtained from a ring compression test (RCT).

Supplementary Files

This is a list of supplementary files associated with this preprint. Click to download.

- NRICH.m